



# Dual H<sub>2</sub>O<sub>2</sub> production paths over chemically etched MoS<sub>2</sub>/FeS<sub>2</sub> heterojunction: Maximizing self-sufficient heterogeneous Fenton reaction rate under the neutral condition

Yang Yang<sup>a</sup>, Haochen Yu<sup>a</sup>, Maoquan Wu<sup>a</sup>, Tingting Zhao<sup>b</sup>, Yina Guan<sup>b</sup>, Dong Yang<sup>a</sup>, Yufeng Zhu<sup>a</sup>, Yanqiu Zhang<sup>b</sup>, Shouchun Ma<sup>a</sup>, Jie Wu<sup>b,\*</sup>, Li Liu<sup>a,\*</sup>, Tongjie Yao<sup>a,\*</sup>

<sup>a</sup> State Key Laboratory of Urban Water Resource and Environment, School of Chemistry and Chemical Engineering, Harbin Institute of Technology, Harbin, P.R. China

<sup>b</sup> Key Laboratory of Functional Inorganic Material Chemistry, Ministry of Education, School of Chemistry and Materials Science, Heilongjiang University, Harbin, P.R. China

## ARTICLE INFO

### Keywords:

Photocatalytic reaction  
Fenton reaction  
H<sub>2</sub>O<sub>2</sub> yield  
Sulfur vacancy  
Hydroxyl group

## ABSTRACT

Sufficient generation of H<sub>2</sub>O<sub>2</sub> played an essential role in boosting self-sufficient heterogeneous Fenton reaction. Herein, the dual H<sub>2</sub>O<sub>2</sub> production paths were designed to maximize the yield over H<sub>2</sub>O<sub>2</sub>-etched MoS<sub>2</sub>/FeS<sub>2</sub> Z-scheme heterojunction, whose surface was modified with abundant –OH groups and sulfur vacancies (SVs). Mechanism studies revealed that H<sub>2</sub>O<sub>2</sub> was generated via two-step single-electron reduction by electrons on conduction band, where H<sub>2</sub>O<sub>2</sub> production was significantly improved by the internal hole-scavenging effect from –OH groups. Additionally, electrons surrounding SVs served as another sites for H<sub>2</sub>O<sub>2</sub> production via one-step two-electron reduction even in darkness. H<sub>2</sub>O<sub>2</sub> yield in neutral aqueous solution reached 1.5 mM/g/h without external hole scavenger. Tetracycline and rhodamine B were effectively degraded under light or in darkness. The degradation performance was even comparable to the heterogeneous Fenton reaction. This work provides new insights for the design of self-sufficient heterogeneous Fenton system with exceptional degradation performance.

## 1. Introduction

Fenton reaction has drawn the increasing attention in the field of non-selective pollutant degradation, where the •OH with powerful oxidizing capacity are produced via H<sub>2</sub>O<sub>2</sub> activation [1–3]. In homogeneous/heterogeneous Fenton reaction, the external H<sub>2</sub>O<sub>2</sub> is needed to be continuously fed to sustain the degradation reaction. This not only raises the cost, but also poses the potential safety hazard due to the explosive nature [4]. Moreover, it is reported that the utilization efficiency of H<sub>2</sub>O<sub>2</sub> was poor via the external feeding mode [5].

To address these problems, a cascade reaction, well-known as the self-sufficient Fenton reaction, has been proposed, where H<sub>2</sub>O<sub>2</sub> is *in-situ* produced inside the system via photocatalytic synthesis, and then directly functions as oxidant in subsequent Fenton reaction [6–8]. Most studies were focused on initiating the Fenton reaction through external addition of Fe<sup>3+</sup>/Fe<sup>2+</sup> ions [9–11]. In this case, the intrinsic drawbacks of homogeneous Fenton reaction, including the production of iron-slurry and pre-regulation of solution pH, were still unsolved.

As an alternative, self-sufficient heterogeneous Fenton (SSHF) reac-

tion has been explored, where photocatalytic H<sub>2</sub>O<sub>2</sub> production and heterogeneous Fenton reaction are coupled together [12–14]. This is a quite complex reaction, since Fe-based materials not only catalyze the heterogeneous Fenton reaction, but also function as the photocatalyst for H<sub>2</sub>O<sub>2</sub> production. Considering that Fe-based materials usually display outstanding catalytic performance toward the H<sub>2</sub>O<sub>2</sub> activation [15,16], the H<sub>2</sub>O<sub>2</sub> production process becomes the rate-limiting step. Up to now, the degradation performance of SSHF could not comparable to the heterogeneous Fenton reaction, due to the insufficient *in-situ* H<sub>2</sub>O<sub>2</sub> yield. Besides, the maximum degradation rate for heterogeneous Fenton reaction is usually realized under the acidic environment [17–19]. In this case, the metal leaching and the pre-adjusting of pH values pose great challenges to large-scale application. Therefore, it is highly desirable to explore an effective technique for pollutant degradation under the neutral condition.



\* Corresponding authors.

E-mail addresses: [wujie@hlju.edu.cn](mailto:wujie@hlju.edu.cn) (J. Wu), [liuli@hit.edu.cn](mailto:liuli@hit.edu.cn) (L. Liu), [yaotj@hit.edu.cn](mailto:yaotj@hit.edu.cn) (T. Yao).

<https://doi.org/10.1016/j.apcatb.2022.122307>

Received 20 October 2022; Received in revised form 16 December 2022; Accepted 17 December 2022

Available online 21 December 2022

0926-3373/© 2022 Elsevier B.V. All rights reserved.

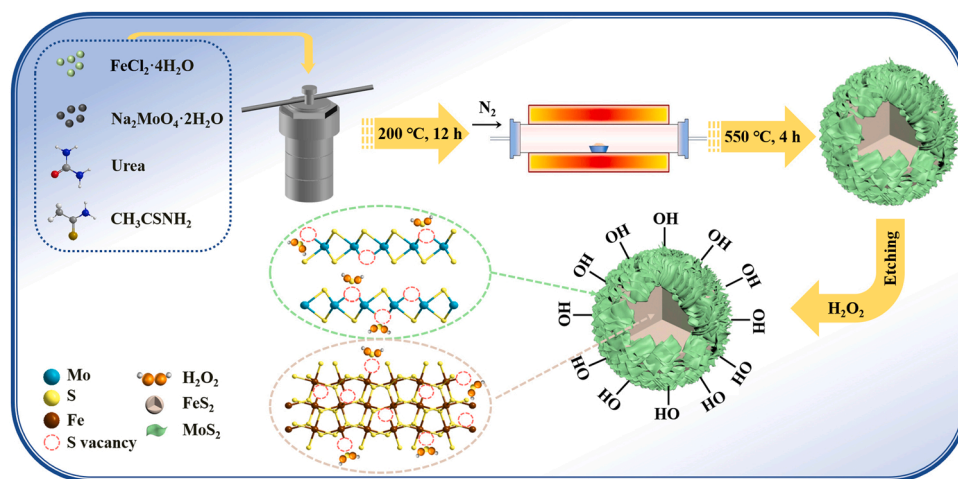


Fig. 1. Synthesis process of E-MoS<sub>2</sub>/FeS<sub>2</sub>.



According to Eqs. 1–3, H<sub>2</sub>O<sub>2</sub> is synthesized via photocatalytic reduction of O<sub>2</sub> and H<sup>+</sup> by electron (e<sup>-</sup>) [20,21]. Therefore, the separation efficiency of hole-electron pairs becomes quite important. To this end, organic chemicals (e.g., ethyl alcohol, methanol, and isopropanol) are usually acted as external hole (h<sup>+</sup>) scavengers to release more e<sup>-</sup> [22]. However, this is not a satisfying solution, since organics compete with targeted pollutant for •OH in Fenton reaction, leading to a lowered degradation efficiency. Some studies demonstrated that -OH groups bonded on the photocatalyst surface could create an internal h<sup>+</sup>-scavenging effect, by which the characteristic time for trapping h<sup>+</sup> is shortened to only 100 fs, much faster than that of hole-electron pairs recombination (10 ps) [23]. As a result, more e<sup>-</sup> can be separated from the hole-electron pairs for H<sub>2</sub>O<sub>2</sub> production. For example, Chen et al. reported that chemically-bonded diethylene glycol on TiO<sub>2</sub> surface promoted internal h<sup>+</sup>-scavenging effect and high e<sup>-</sup>-releasing capacity for Cr(VI) reduction [23]. Jiang et al. reported that -OH-rich BiOCl showed more efficient interfacial charge transfer than that of pristine BiOCl [24].

Although H<sub>2</sub>O<sub>2</sub> yield can be improved with the help of internal h<sup>+</sup>-scavenging effect, their production still completely relies on the photocatalytic process. To maximize the yield, other production path should be explored. Vacancies on catalyst surface are famous for high surrounding electron density, and many reduction reaction can take place around the vacancies. For example, Wang et al. reported that oxygen vacancies on porous Co<sub>3</sub>O<sub>4</sub> nanosheet surface showed outstanding NO reduction performance [25]. Li et al. reported that sulfur vacancies (SVs) on MoS<sub>2</sub> surface prompted the hydrogen evolution [26]. Therefore, it is rational to infer that vacancies can be served as another active sites for H<sub>2</sub>O<sub>2</sub> generation, and the generation process is independent with light irradiation.

Based on above statements, herein, a Z-scheme MoS<sub>2</sub>/FeS<sub>2</sub> heterojunction with a core/shell structure was firstly prepared. Then, SVs and -OH groups were engineered on the heterojunction (E-MoS<sub>2</sub>/FeS<sub>2</sub>) surface through an etching process by pre-prepared H<sub>2</sub>O<sub>2</sub> (H<sub>2</sub>O<sub>2(pre)</sub>) solution. E-MoS<sub>2</sub>/FeS<sub>2</sub> formation mechanism and surface engineering process were characterized by X-ray photoelectron spectrum (XPS), O<sub>2</sub> temperature-programmed desorption (O<sub>2</sub>-TPD), and electron paramagnetic resonance (EPR) measurements. The kinetics of both H<sub>2</sub>O<sub>2</sub> production process and pollutant degradation process were investigated, and the SSHF reaction displayed the best performance toward tetracycline (TC) degradation under the neutral condition. Mechanism studies revealed that H<sub>2</sub>O<sub>2</sub> were produced on E-MoS<sub>2</sub>/FeS<sub>2</sub> heterojunction surface via dual paths: two-step single-electron reduction by e<sup>-</sup> on the conduction band (CB) of FeS<sub>2</sub>, and one-step two-electron reduction by e<sup>-</sup>

surrounding SVs. The positive role of internal h<sup>+</sup>-scavenging effect from surface modified -OH groups was revealed, and the contributions of possible active species for TC degradation were determined by EPR measurement, radical trapping experiment, and photo-electrochemical measurement. As a result, the complex SSHF reaction mechanism, including e<sup>-</sup> transfer path, H<sub>2</sub>O<sub>2</sub> production path, and pollutant degradation path, were clearly illustrated. This study provided a new perspective for preparation of SSHF catalysts by maximizing the *in-situ* generated H<sub>2</sub>O<sub>2</sub> yield. Benefiting from the high H<sub>2</sub>O<sub>2</sub> production performance, the degradation performance of SSHF reaction could be comparable to the heterogeneous Fenton reaction.

## 2. Experiment

### 2.1. Chemicals

FeCl<sub>2</sub>·4H<sub>2</sub>O, Na<sub>2</sub>MoO<sub>4</sub>·2H<sub>2</sub>O, NaH<sub>2</sub>PO<sub>4</sub>, Na<sub>2</sub>CO<sub>3</sub>, NaHCO<sub>3</sub>, NaNO<sub>3</sub>, Na<sub>2</sub>SO<sub>4</sub>, NaCl, AgNO<sub>3</sub>, H<sub>2</sub>O<sub>2</sub> (30 wt %), potassium titanium oxalate, thioacetamide, urea, catalase, rhodamine B (RhB), methanol (MeOH), terephthalic acid (TPA), triethanolamine (TEOA), tetracycline (TC), *tert*-butyl alcohol (TBA), *p*-benzoquinone (BQ), nitroterrazolium blue chloride (NBT), 5,5-Dimethyl-1-pyrroline N-oxide (DMPO), 2,2,6,6-tetramethylpiperidine-1-oxyl (TEMPO), and ethanol were purchased from China Pharmaceutical Chemical Reagent Co., Ltd. All of the chemicals were analytical grade and used as received. The deionized water was purified through a Millipore system with a resistivity of 18.2 MΩ·cm<sup>-1</sup>.

### 2.2. Preparation of MoS<sub>2</sub>/FeS<sub>2</sub>

Firstly, 1.9 g/L of Na<sub>2</sub>MoO<sub>4</sub>·2H<sub>2</sub>O, 5.0 g/L of thioacetamide, and 22.5 g/L of urea were dissolved into the mixture of H<sub>2</sub>O (53.3 mL) and ethanol (26.7 mL). Then, 1.9 g/L of FeCl<sub>2</sub>·4H<sub>2</sub>O was added into the mixture under ultrasound. Subsequently, the mixture was transferred to a Teflon-lined stainless-steel autoclave and heated at 200 °C for 12.0 h. After washing by water and ethanol, the as-obtained products were annealed at 550 °C for 4.0 h under N<sub>2</sub> atmosphere with a heating rate of 5 °C/min. A similar procedure was used to prepare pure MoS<sub>2</sub> or pure FeS<sub>2</sub> except that FeCl<sub>2</sub>·4 H<sub>2</sub>O or Na<sub>2</sub>MoO<sub>4</sub>·2H<sub>2</sub>O was absence.

### 2.3. Etching the MoS<sub>2</sub>/FeS<sub>2</sub> by H<sub>2</sub>O<sub>2(pre)</sub>

The synthetic procedure of E-MoS<sub>2</sub>/FeS<sub>2</sub> is shown in Fig. 1. In this process, the commercial H<sub>2</sub>O<sub>2</sub> (30 wt %) was used as the etchant. To distinguish the commercial H<sub>2</sub>O<sub>2</sub> from the self-generated H<sub>2</sub>O<sub>2</sub> in SSHF reaction, the commercial H<sub>2</sub>O<sub>2</sub> solution was assigned as pre-prepared H<sub>2</sub>O<sub>2</sub> (H<sub>2</sub>O<sub>2(pre)</sub>). Typically, the as-obtained MoS<sub>2</sub>/FeS<sub>2</sub> was soaked in

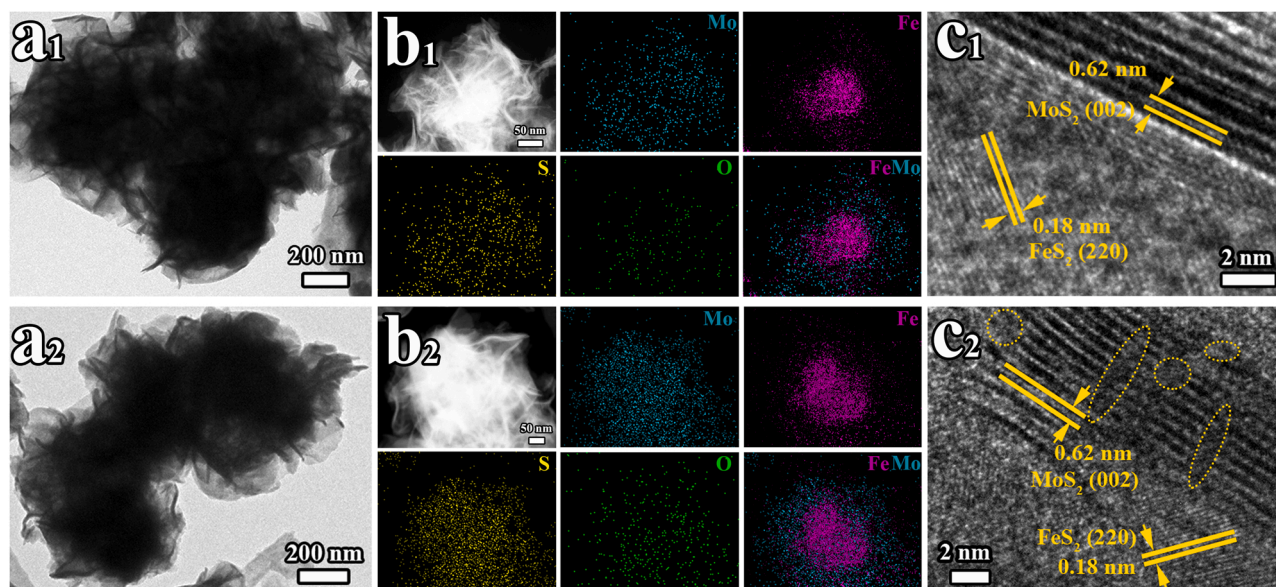
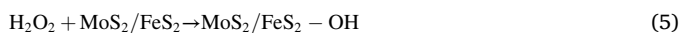


Fig. 2. (a) TEM, (b) elemental mapping, and (c) HRTEM images of: (a<sub>1</sub>, b<sub>1</sub>, c<sub>1</sub>) MoS<sub>2</sub>/FeS<sub>2</sub>, (a<sub>2</sub>, b<sub>2</sub>, c<sub>2</sub>) E-MoS<sub>2</sub>/FeS<sub>2</sub>.

0.5 M of H<sub>2</sub>O<sub>2</sub>(pre) solution for 5.0 min. After washing by deionized water, the products were dried in an oven for a night, and E-MoS<sub>2</sub>/FeS<sub>2</sub> with abundant SVs and oxygenic groups on the surface was prepared (Eqs. 4–5).



#### 2.4. TC degradation

Photocatalytic reaction was performed on a photochemical reaction system (HSX-F/UV 300), and a 300 W xenon lamp with a 400 nm cut-filter was used as a visible light source. TC degradation was selected as a model reaction to evaluate the catalytic performance under different experimental conditions, and the reaction temperature was kept at 25 °C by a circulating water system. For a typical degradation reaction, 0.16 g/L of catalyst was added into 50 mL of TC solution (25 mg/L) under mechanical stirring in darkness for 30 min to establish the adsorption-desorption equilibrium. After tuning on the xenon lamp, SSHF reaction was initiated. During the degradation process, 2.0 mL of solution was sampled at the given time interval. After removing the catalyst via centrifugation, the supernate absorbance at 357 nm was immediately measured by a UV–vis spectrometer (Labtech, UV-9100B) to determine the TC concentration [27], and the test result was examined by high performance liquid chromatography (HPLC, Figs. S1a–S1c). Based on the pseudo first-order kinetics equation, *k* of various catalysts were calculated.

#### 2.5. H<sub>2</sub>O<sub>2</sub> generation

To measure the concentration of H<sub>2</sub>O<sub>2</sub> generated in SSHF reaction, the reaction system was maintained the same as that for TC degradation, except TC aqueous solution was replaced by aqueous solution. The concentration of *in-situ* generated H<sub>2</sub>O<sub>2</sub> was determined using potassium titanium colorimetric method. Potassium titanium oxalate was used as a chromogenic reagent, and the solution absorbance was detected by a UV–vis spectrometer at 400 nm (Fig. S1d).

#### 2.6. Characterization

The crystalline phase of the samples was characterized by X-ray

diffraction (XRD) using a Smartlab apparatus (CuK<sub>α</sub> radiation,  $\lambda = 1.5418 \text{ \AA}$ ,  $2\theta = 10\text{--}80^\circ$ ). The morphology and microstructure were characterized by scanning electron microscope (SEM, Hitachi S4800), transmission electron microscope (TEM, JEOL JEM-2100), high-resolution TEM (HRTEM) and elemental mappings. XPS and valence band (VB) XPS were measured on a VG ESCALAB MKII X-ray photoelectron spectrometer with MgK<sub>α</sub> excitation (1253.6 eV). Brunauer-Emmett-Teller (BET) specific surface area was obtained by measuring N<sub>2</sub> adsorption-desorption with a Beckman Coulter 3100 pore size and surface area analyzer. Raman spectroscopy (Renishaw inVia) was used to obtain chemical shift and elemental composition with a 524.5 nm Ar<sup>+</sup> laser at room temperature. The water contact angle was measured by Contact Angle Tester (JY-82, DINGSHENG, China). Inductively coupled plasma atomic spectroscopy (ICP) was performed on an Optima 7000 DV. The mineralization of TC was tested by a total organic carbon analyzer (TOC-VCPH/CPN, Shimadzu, Japan). O<sub>2</sub>-TPD was obtained by TP-5079 apparatus (China). UV–vis diffuse reflection spectroscopy (UV–vis DRS) was obtained using a Scan UV–vis spectrophotometer (UV-2450, Shimadzu, Japan) equipped with an integrating sphere assembly, using BaSO<sub>4</sub> as reflectance sample. EPR spectroscopy was tested on a Bruker A200 spectrometer. Photoluminescence (PL) spectroscopy was measured using a PTI QM-4 fluorescence spectrophotometer. Cyclic voltammetry (CV) measurement, electrochemical impedance spectroscopy (EIS) measurement, and photocurrent measurement were conducted on a Chenhua CHI 760E electrochemical workstation with a three-electrode cell. The working electrode was prepared by coating the sample on FTO glass, and then placing into a vacuum oven at 50 °C for 2.0 h. Platinum gauze and an Ag/AgCl electrode were used as the counter electrode and reference electrode. NaCl solution was used as the electrolyte. Scanning Kelvin probe (SKP) measurement was performed on a SKP5050 system. The degradation intermediates of TC were identified by high performance liquid chromatography coupled to micro TOF-Q II time-of-flight mass spectrometry (HPLC-MS, Agilent 1260 HPLC/Bruker microTOF-Q II).

### 3. Results and discussion

#### 3.1. Structure and composition

Similar to MoS<sub>2</sub>/FeS<sub>2</sub>, E-MoS<sub>2</sub>/FeS<sub>2</sub> also presents a flower-like morphology composed of numerous thin nanosheets (Figs. S2, 2a<sub>1</sub>, and 2a<sub>2</sub>). In the corresponding elemental mappings before and after



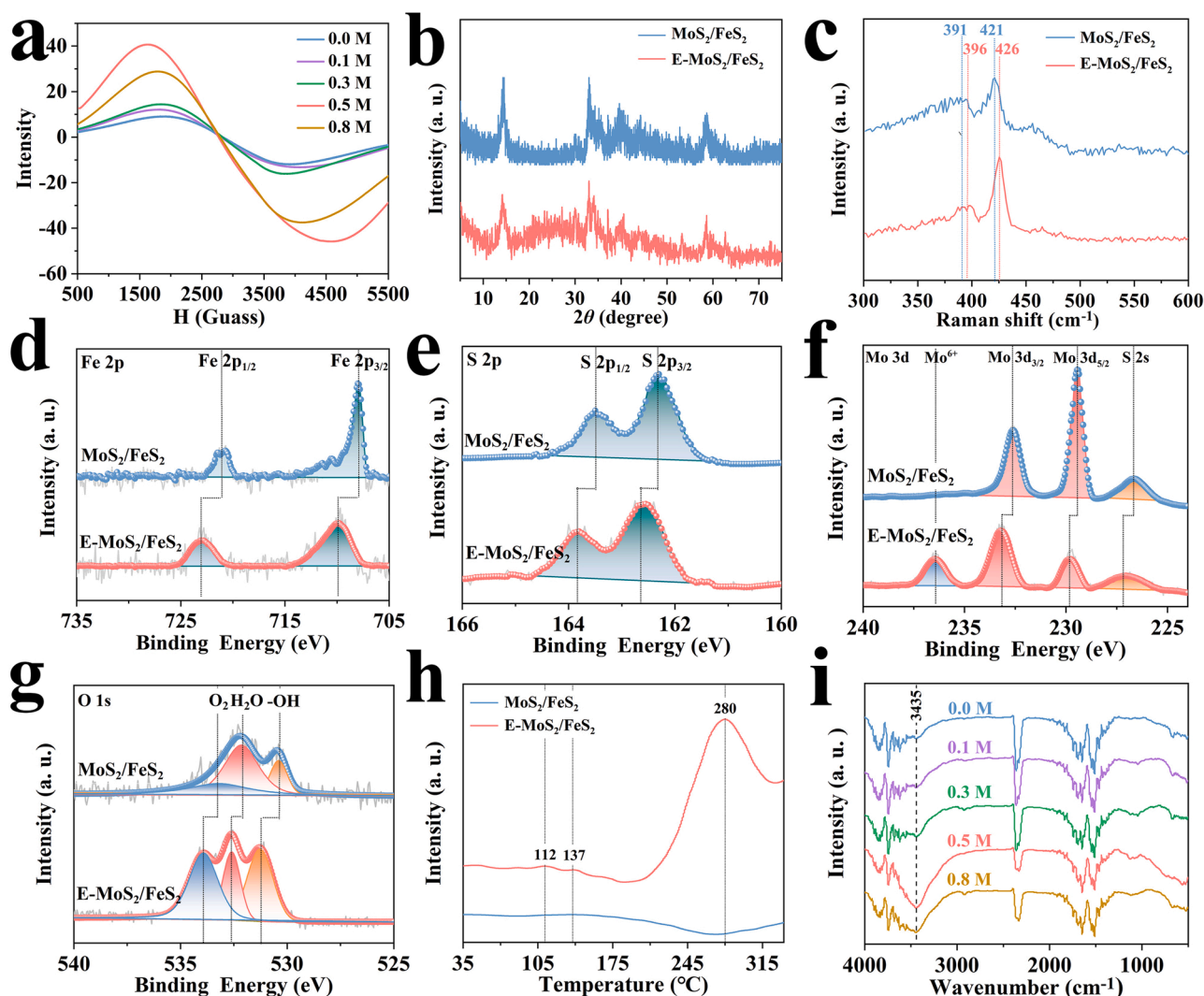


**Fig. 3.** (a) EPR and (i) FTIR spectra over E-MoS<sub>2</sub>/FeS<sub>2</sub> prepared with different H<sub>2</sub>O<sub>2</sub>(pre) concentrations. (b) XRD patterns, (c) Raman spectra, (d) core-level spectra of Fe 2p, (e) core-level spectra of S 2p, (f) core-level spectra of Mo 3d, (g) core-level spectra of O 1s, and (h) O<sub>2</sub>-TPD curves over MoS<sub>2</sub>/FeS<sub>2</sub> and E-MoS<sub>2</sub>/FeS<sub>2</sub>.

etching (Figs. 2b<sub>1</sub> and 2b<sub>2</sub>), the elements Mo and S are uniformly dispersed over the whole composite, while the element Fe is mainly concentrated in the core region, confirming the formation of core/shell structure. The notable difference between these two samples is that the element O emerges in E-MoS<sub>2</sub>/FeS<sub>2</sub>, while it is absent in MoS<sub>2</sub>/FeS<sub>2</sub> (Fig. S3). This suggests plenty of oxygenic groups are generated on E-MoS<sub>2</sub>/FeS<sub>2</sub> surface during the etching process. As shown in Fig. S4, the pore sizes of MoS<sub>2</sub>/FeS<sub>2</sub> and E-MoS<sub>2</sub>/FeS<sub>2</sub> are mainly distributed in the range of 2–50 nm, indicating the existence of mesopores. The surface area of E-MoS<sub>2</sub>/FeS<sub>2</sub> is 25 m<sup>2</sup>/g, which is about 2.1 times higher than that of MoS<sub>2</sub>/FeS<sub>2</sub> (12 m<sup>2</sup>/g). High-resolution TEM (HRTEM) image is taken at the interface (Figs. 2c<sub>1</sub> and 2c<sub>2</sub>), where two kinds of lattice fringes with distance values of 0.62 and 0.18 nm are observed, corresponding to the (002) plane of MoS<sub>2</sub> and the (220) plane of FeS<sub>2</sub>, respectively. Particular attention has been paid to the MoS<sub>2</sub> shell. Compared to the integrated crystal lattice of MoS<sub>2</sub> shell in MoS<sub>2</sub>/FeS<sub>2</sub>, the dislocations and distortions are widely distributed in E-MoS<sub>2</sub>/FeS<sub>2</sub> (Fig. 2c<sub>2</sub>), indicating abundant defects are generated during the etching process.

XPS measurement was carried out to determine the defect types. The atomic ratio of Mo/S increases from 1.0:1.8 to 1.0:1.0 after etching (Table S1), suggesting lattice S is removed and SVs are generated on the MoS<sub>2</sub> surface via surface engineering. EPR analysis was a powerful technique to detect various vacancies, and the signal intensity was

proportional to the vacancy amount [28–30]. In Fig. 3a, the signal at  $g = 2.003$  confirms the existence of SVs in E-MoS<sub>2</sub>/FeS<sub>2</sub>. With increasing the H<sub>2</sub>O<sub>2</sub>(pre) concentrations from 0.0 to 0.5 M, the signal intensities gradually enhance, indicating the increased SVs amount. Further increasing the concentration to 0.8 M, the signal intensity decreases due to the structural destruction. Therefore, SVs were generated by H<sub>2</sub>O<sub>2</sub>(pre) etching (Eq. 4), and their amount could be controlled by H<sub>2</sub>O<sub>2</sub>(pre) concentrations.

In XRD pattern of MoS<sub>2</sub>/FeS<sub>2</sub> (Fig. 3b), four diffraction peaks at 14.4, 33.5, 39.5, and 58.3° correspond to (002), (100), (103), and (110) lattice planes of MoS<sub>2</sub> (JCPDS NO. 37-1492). Two additional peaks emerge at 32.9 and 37.1° are indexed to the (200) and (210) planes of FeS<sub>2</sub> (JCPDS NO. 42-1340). Compared to MoS<sub>2</sub>/FeS<sub>2</sub>, the diffraction peak positions of E-MoS<sub>2</sub>/FeS<sub>2</sub> are unchanged, indicating the negligible influence on the crystal phase during the etching process. In Raman spectrum of MoS<sub>2</sub>/FeS<sub>2</sub> (Fig. 3c), A<sub>1g</sub> phonon mode of MoS<sub>2</sub> appears at 421 cm<sup>-1</sup>, while the characteristic A<sub>g</sub> peak of FeS<sub>2</sub> at 384 cm<sup>-1</sup> is overlapped by E<sub>2g</sub> peak of MoS<sub>2</sub> at 391 cm<sup>-1</sup> [31,32]. After etching, E<sub>2g</sub> peak and A<sub>1g</sub> peak respectively shift from 391 to 396 cm<sup>-1</sup>, and from 421 to 426 cm<sup>-1</sup> due to the generation of SVs.

The variation of surface composition before and after etching was investigated by XPS spectra. In comparison with MoS<sub>2</sub>/FeS<sub>2</sub>, the binding energies of Mo 3d, Fe 2p, S 2p and O 1s in E-MoS<sub>2</sub>/FeS<sub>2</sub> remarkably red-shift owing to the H<sub>2</sub>O<sub>2</sub>(pre) oxidation (Figs. 3d–3g). For E-MoS<sub>2</sub>/FeS<sub>2</sub>,



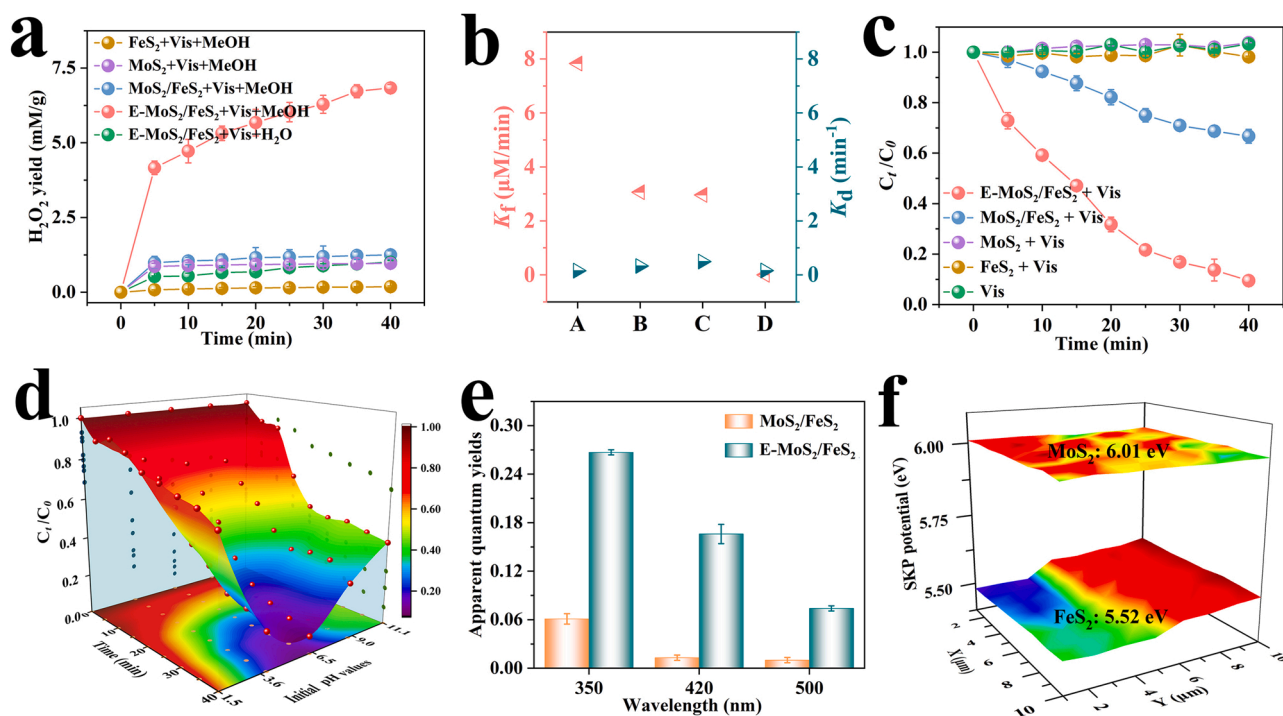


**Fig. 4.** (a) H<sub>2</sub>O<sub>2</sub> yield over various catalysts. (b)  $K_f$  and  $K_d$  for H<sub>2</sub>O<sub>2</sub> generation: (A) E-MoS<sub>2</sub>/FeS<sub>2</sub>, (B) MoS<sub>2</sub>/FeS<sub>2</sub>, (C) MoS<sub>2</sub>, (D) FeS<sub>2</sub>. (c) Degradation efficiencies of TC over various catalysts. (d) Degradation performance over E-MoS<sub>2</sub>/FeS<sub>2</sub> under different initial pH values. (e) AQY of MoS<sub>2</sub>/FeS<sub>2</sub> and E-MoS<sub>2</sub>/FeS<sub>2</sub> under different monochromatic light. (f) SKP maps of MoS<sub>2</sub> and FeS<sub>2</sub>. Reaction condition: catalyst = 0.16 g/L, 50 mL [TC]<sub>0</sub> = 25 mg/L and initial pH = 6.5.

the core-level spectrum of Fe 2p shows the two peaks at 723.0 (Fe 2p<sub>1/2</sub>) and 709.9 eV (Fe 2p<sub>3/2</sub>), and the doublet peaks at 163.9 and 162.7 eV correspond to S 2p<sub>1/2</sub> and S 2p<sub>3/2</sub>. In Mo 3d spectrum, the two peaks at 233.2 and 229.8 eV respectively correspond to Mo 3d<sub>3/2</sub> and Mo 3d<sub>5/2</sub> of Mo<sup>4+</sup>. The peak of Mo<sup>6+</sup> at 236.5 eV emerges in E-MoS<sub>2</sub>/FeS<sub>2</sub> owing to the reactions between MoS<sub>2</sub>/FeS<sub>2</sub> and H<sub>2</sub>O<sub>2(pre)</sub>: on the one hand, Fe<sup>2+</sup> reacted with H<sub>2</sub>O<sub>2(pre)</sub> for Fe<sup>3+</sup>. On the other hand, Fe<sup>3+</sup> was reduced to Fe<sup>2+</sup> by Mo<sup>4+</sup>, and Mo<sup>4+</sup> itself was oxidized to Mo<sup>6+</sup> (Eqs. 6–7).



In O 1s spectrum, the peaks at 532.6, 533.9 and 531.2 eV correspond to the adsorbed H<sub>2</sub>O, adsorbed O<sub>2</sub> and surface-bonded -OH groups, respectively. The content of adsorbed H<sub>2</sub>O decreases after etching, while the contents of adsorbed O<sub>2</sub> and -OH groups increase from 30.0 % to 41.1 %, and from 14.3 % to 36.0 % (Table S1). Besides XPS analysis, the amount of oxygenic species on sample surface was investigated by O<sub>2</sub>-TPD measurement. At a low temperature region ( $T < 200$  °C, Fig. 3h), MoS<sub>2</sub>/FeS<sub>2</sub> shows a weak peak, whereas E-MoS<sub>2</sub>/FeS<sub>2</sub> displays two strong peaks, indicating the higher concentration of physically-adsorbed O<sub>2</sub>. At the moderate temperature region ( $200$  °C  $< T < 300$  °C), E-MoS<sub>2</sub>/FeS<sub>2</sub> exhibits a pronounced peak at 280 °C, confirming a large amount of -OH groups are modified via H<sub>2</sub>O<sub>2(pre)</sub> etching (Eq. 5). For contrast, few -OH groups are modified on the MoS<sub>2</sub>/FeS<sub>2</sub> surface. The increased number of hydrophilic -OH groups is further verified by the surface wettability variation (Fig. S5), and the water contact angel decreases from  $58 \pm 2^\circ$  (MoS<sub>2</sub>/FeS<sub>2</sub>) to  $38 \pm 2^\circ$  (E-MoS<sub>2</sub>/FeS<sub>2</sub>). To determine the relationship between the -OH numbers and the H<sub>2</sub>O<sub>2(pre)</sub> concentrations, FTIR spectra were carried out by comparing the peak intensity of -OH group at 3435 cm<sup>-1</sup>. With the increased H<sub>2</sub>O<sub>2(pre)</sub> concentrations, the peak intensity increases at the beginning, and then sharply reduce, with a maximum value at 0.5 M (Fig. 3i).

### 3.2. TC degradation performance in SSHF reaction

SSHF reaction was recognized as a cascade reaction composed of photocatalytic H<sub>2</sub>O<sub>2</sub> production and subsequent heterogeneous Fenton reaction, where the *in-situ* generated H<sub>2</sub>O<sub>2</sub> was functioned as the oxidant for Fenton reaction. Therefore, the H<sub>2</sub>O<sub>2</sub> production performance were firstly investigated, and then TC degradation efficiency in Fenton reaction was evaluated.

#### 3.2.1. H<sub>2</sub>O<sub>2</sub> production performance

The H<sub>2</sub>O<sub>2</sub> production performance was investigated under visible light in MeOH solution (75 vol %, Fig. 4a), where MeOH was served as the *h*<sup>+</sup> scavenger [33]. The yield over E-MoS<sub>2</sub>/FeS<sub>2</sub> is 10.2 mM/g/h, about 36.6, 7.1 and 5.5 times higher than those of FeS<sub>2</sub>, MoS<sub>2</sub> and MoS<sub>2</sub>/FeS<sub>2</sub>, respectively. The photocatalytic H<sub>2</sub>O<sub>2</sub> performance of E-MoS<sub>2</sub>/FeS<sub>2</sub> in aqueous solution was also studied, and the yield was 1.5 mM/g/h. Table S2 lists the recent reports on photocatalytic H<sub>2</sub>O<sub>2</sub> production. E-MoS<sub>2</sub>/FeS<sub>2</sub> presents the highest H<sub>2</sub>O<sub>2</sub> yield in both MeOH solution and aqueous solution, even under the simultaneous decomposition via a Fenton reaction.

The formation rate constant ( $K_f$ ) and decomposition rate constant ( $K_d$ ) in H<sub>2</sub>O<sub>2</sub> production process were calculated based on the zero-order kinetics and first-order kinetics (Eq. 8) [34], and the data are shown in Fig. 4b. The  $K_d$  values for these four samples are similar, while the  $K_f$  value for E-MoS<sub>2</sub>/FeS<sub>2</sub> is 7.8 μM/min, about 78.0, 2.7 and 2.5 times higher than those of FeS<sub>2</sub>, MoS<sub>2</sub> and MoS<sub>2</sub>/FeS<sub>2</sub>, respectively. Therefore, E-MoS<sub>2</sub>/FeS<sub>2</sub> displays the best H<sub>2</sub>O<sub>2</sub> production performance.

$$[\text{H}_2\text{O}_2] = \frac{K_f}{K_d} (1 - \exp(-K_d t)) \quad (8)$$

#### 3.2.2. TC degradation performance

TC, the second most produced antibiotic, posed a severe threat to human health and ecological environment, since it showed high toxicity to the stomach, kidney, liver and metabolic system. It is highly desirable to develop a technique for their effective disposal. Here, TC degradation

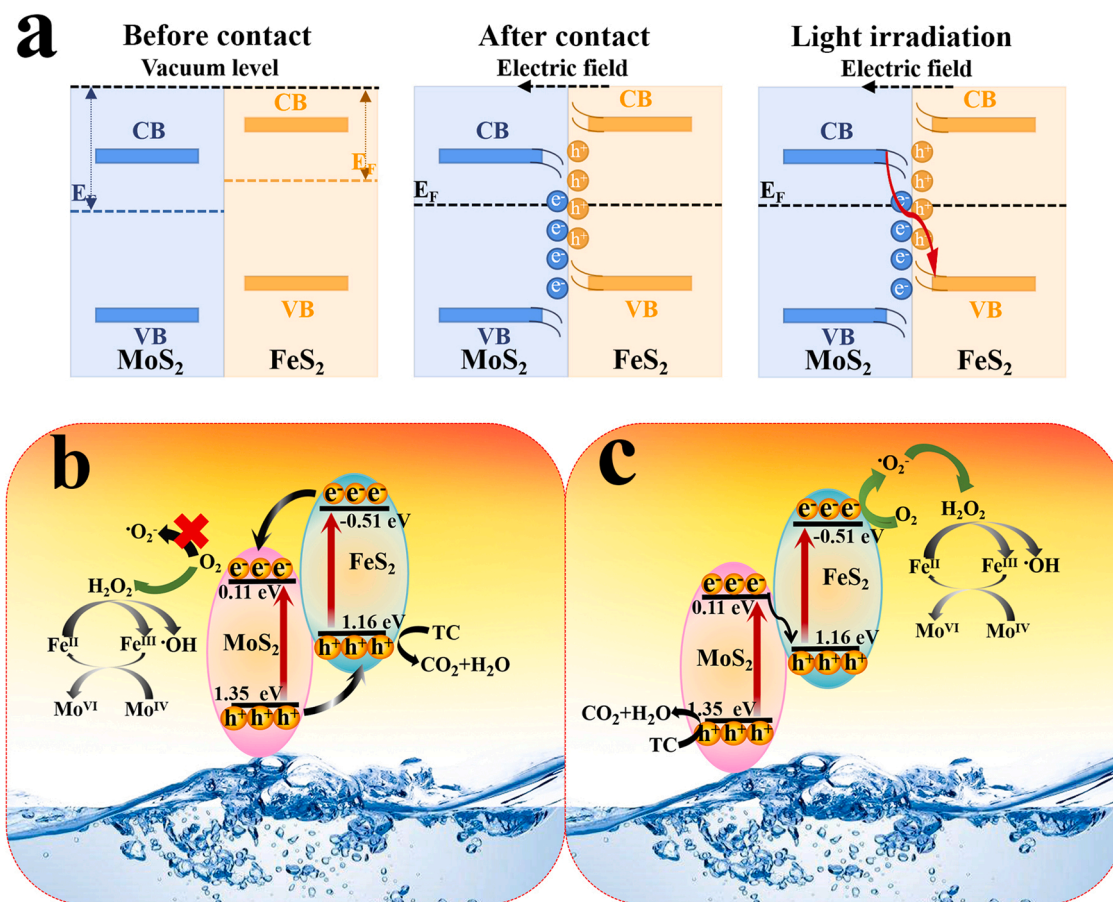


Fig. 5. (a) Internal-electric-field inside the E-MoS<sub>2</sub>/FeS<sub>2</sub>. Schematic illustration of photocatalytic mechanism: (b) type-II routine and (c) Z-scheme routine.

was selected as a model reaction to evaluate the catalytic performance. As shown in Fig. 4c, the degradation efficiency of TC is negligible in the presence of visible light (Vis) but the absence of catalysts. TC is hardly degraded in FeS<sub>2</sub> + Vis system due to the negligible H<sub>2</sub>O<sub>2</sub> yield. Although H<sub>2</sub>O<sub>2</sub> was generated in MoS<sub>2</sub> + Vis system, little TC is degraded due to the inferior activity of MoS<sub>2</sub> in Fenton reaction [1]. In MoS<sub>2</sub>/FeS<sub>2</sub> + Vis system, the degradation efficiency is 33.3 %. For comparison, 90.6 % of TC is degraded in E-MoS<sub>2</sub>/FeS<sub>2</sub> + Vis system, and the corresponding *k* value is  $5.9 \times 10^{-2} \text{ min}^{-1}$ , about 5.3 times higher than that of MoS<sub>2</sub>/FeS<sub>2</sub> + Vis system. Moreover, the mineralization efficiency of E-MoS<sub>2</sub>/FeS<sub>2</sub> + Vis system (56.7 %) is 4.7 times higher than MoS<sub>2</sub>/FeS<sub>2</sub> + Vis system (12.1 %), and the detailed mineralization path is analyzed by HPLC-MS measurement (Fig. S6). The outstanding activity of E-MoS<sub>2</sub>/FeS<sub>2</sub> is confirmed by CV curves (Fig. S7), where E-MoS<sub>2</sub>/FeS<sub>2</sub> displays the highest current intensity, indicating the largest amount of transferred *e*<sup>-</sup> in degradation process. Table S3 lists some reports on photocatalytic reaction, photo-Fenton reaction, and self-sufficient Fenton reaction, where E-MoS<sub>2</sub>/FeS<sub>2</sub> displays the best performance.

### 3.2.3. SSHF reaction under different initial pH values

TC degradation efficiencies under different initial pH values in SSHF reaction were studied (Fig. 4d). When the initial pH values increase from 1.5 to 6.5, the degradation efficiencies at 40 min increase from 31.5 % to 90.6 %. Further increasing the pH values to 9.0 and 11.1, the efficiencies decrease to 70.0 % and 57.9 %. The same tendency is observed in the mineralization efficiency of TC, and E-MoS<sub>2</sub>/FeS<sub>2</sub> displays a maximum efficiency of 56.7 % at the initial solution pH of 6.5 (Fig. S8). This was absolutely different from the heterogeneous Fenton reaction, whose highest degradation performance was in the acidic condition (pH ≈ 3.0) [35–37].

To reveal why SSHF reaction displayed the best degradation performance under the neutral condition, H<sub>2</sub>O<sub>2</sub> yields under different initial pH values were investigated. In Fig. S9, the H<sub>2</sub>O<sub>2</sub> yields increase from 7.3 to 12.6 mM/g/h with the decreased initial pH values from 11.1 to 1.5, owing to the increased [H<sup>+</sup>] (Eqs. 1–3) [38]. Therefore, the TC degradation rate in SSHF reaction was lowered owing to the insufficient H<sub>2</sub>O<sub>2</sub> in the pH range of 6.5–11.5. In Fenton reaction, the degradation rate was not monotonously improved with the increased H<sub>2</sub>O<sub>2</sub> dosage, since the <sup>•</sup>OH could be consumed by excessive H<sub>2</sub>O<sub>2</sub> (Eqs. 9–10) [1,39]. Therefore, we inferred the gradually decreased degradation rate following the decreased initial pH values from 6.5 to 1.5 was due to the quenching effect of over-produced H<sub>2</sub>O<sub>2</sub>. This provided evidence that H<sub>2</sub>O<sub>2</sub> yield on E-MoS<sub>2</sub>/FeS<sub>2</sub> surface was high enough for SSHF reaction. SSHF reaction catalyzed by E-MoS<sub>2</sub>/FeS<sub>2</sub> showed the maximum *k* value under the neutral condition, and this quite satisfied the demands for practical applications, since it not only preserved the high degradation performance, but also avoided the metal leaching under the acidic condition.



### 3.3. Mechanism for SSHF reaction

#### 3.3.1. Photo-electrochemical characterization

UV–vis DRS spectra were tested to illustrate the visible light adsorption property. Compared to FeS<sub>2</sub> and MoS<sub>2</sub>, MoS<sub>2</sub>/FeS<sub>2</sub> displays the higher light absorption (Fig. S10a). After etching, the light harvest is further improved. And this is also confirmed by the superior apparent quantum yield (AQY) values of E-MoS<sub>2</sub>/FeS<sub>2</sub> toward that of MoS<sub>2</sub>/FeS<sub>2</sub>

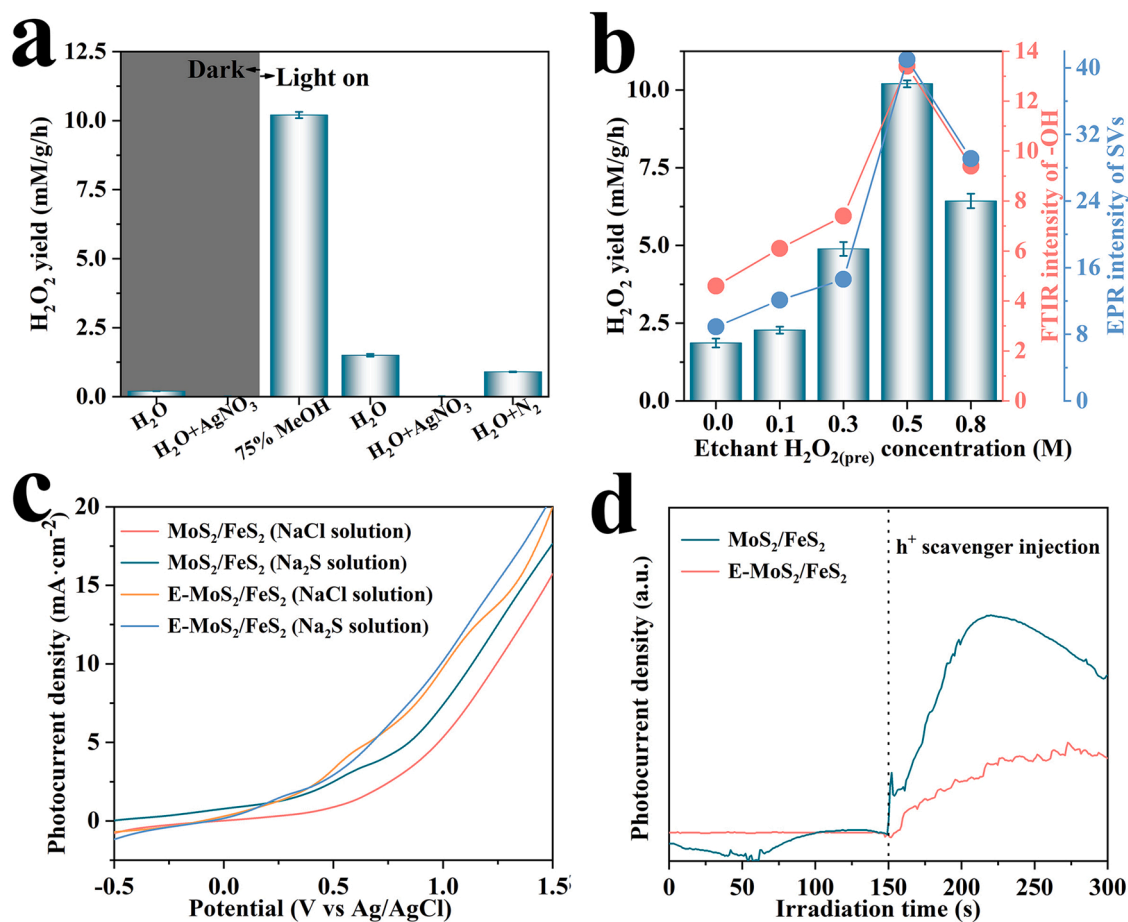


**Fig. 6.** (a) H<sub>2</sub>O<sub>2</sub> yield over E-MoS<sub>2</sub>/FeS<sub>2</sub> under different conditions. (b) Influence of H<sub>2</sub>O<sub>2(pre)</sub> concentrations on H<sub>2</sub>O<sub>2</sub> yield, the amount of modified -OH groups, and the number of SVs. (c) LSV curves and (d) photocurrent responses of different samples under visible light.

(Fig. 4e). Based on the Tauc plot (Fig. S10b), the band-gap energies ( $E_g$ ) of FeS<sub>2</sub> and MoS<sub>2</sub> are calculated to be 1.67 and 1.24 eV, respectively. The VB positions of FeS<sub>2</sub> and MoS<sub>2</sub> are measured to be 1.16 and 1.35 eV (Fig. S10c), and the CB positions are calculated to be -0.51 and 0.11 eV, respectively.

The separation efficiency of photo-induced charge carriers was studied by PL spectra, photocurrent responses, and electrochemical impedance spectra. E-MoS<sub>2</sub>/FeS<sub>2</sub> displays the highest separation efficiency and surface conductivity (Figs. S10d-S10f). For verification, EPR measurement was carried out using TEMPO as the spin trapping agent [40]. In Figs. S11a-S11b, the signal intensities of TEMPO- $h^+$  and TEMPO- $e^-$  in E-MoS<sub>2</sub>/FeS<sub>2</sub> + Vis system are lower than those in MoS<sub>2</sub>/FeS<sub>2</sub> + Vis system, confirming the higher separation efficiency of hole-electron pairs in the former system.

The work functions of MoS<sub>2</sub> and FeS<sub>2</sub> are examined by SKP measurement, and the values are 6.01 and 5.52 eV (Fig. 4f), suggesting the Fermi level of FeS<sub>2</sub> is lower than that of MoS<sub>2</sub>. After contact,  $e^-$  on the CB transferred from FeS<sub>2</sub> to MoS<sub>2</sub> until the Fermi levels reached the same level. As a result, the energy band near the FeS<sub>2</sub> interface bent upward, while the energy band near the MoS<sub>2</sub> interface bent downward. An internal electric field was constructed at the interface, whose direction was from FeS<sub>2</sub> to MoS<sub>2</sub>. Driving by internal electric field,  $e^-$  was like to migrate from CB of MoS<sub>2</sub> to VB of FeS<sub>2</sub> via a Z-scheme path under visible light (Fig. 5a).

The  $e^-$  transfer path was verified by EPR analysis using DMPO as the trapping agent for  $\bullet O_2$  [40]. The signal of DMPO- $\bullet O_2$  is clearly observed under visible light (Fig. S11c). In another experiment, NBT is a famous indicator for  $\bullet O_2$  and 14.4 % of NBT are degraded in E-MoS<sub>2</sub>/FeS<sub>2</sub> + Vis system (Fig. S11d), providing a compelling evidence for  $\bullet O_2$  production

[41]. If  $e^-$  transfers via a type-II path,  $e^-$  and  $h^+$  respectively accumulate on the CB of MoS<sub>2</sub> and the VB of FeS<sub>2</sub> (Fig. 5b). The CB of MoS<sub>2</sub> is 0.11 eV, more positive than  $E_0$  for  $O_2/\bullet O_2$  (-0.33 V/NHE) [42], resulting in unavailability of  $\bullet O_2$  via Eq. 1. This is contradicted with EPR result and NBT experiment. Therefore, Z-scheme transfer path is preferred in E-MoS<sub>2</sub>/FeS<sub>2</sub> heterojunction (Fig. 5c).

### 3.3.2. Mechanism for photocatalytic H<sub>2</sub>O<sub>2</sub> production

Considering the better H<sub>2</sub>O<sub>2</sub> generation performance in MeOH solution than that in aqueous solution, it was rationally inferred that  $e^-$  was involved in the reaction. For verification, a control experiment is performed in the presence of AgNO<sub>3</sub> solution (scavenger for  $e^-$ , Fig. 6a) [43], and H<sub>2</sub>O<sub>2</sub> is scarcely produced under visible light, demonstrating the decisive role of  $e^-$  toward the H<sub>2</sub>O<sub>2</sub> production.

After bubbling by N<sub>2</sub>, H<sub>2</sub>O<sub>2</sub> yield reduces from 1.5 to 0.9 mM/g/h (Fig. 6a), suggesting the dissolved O<sub>2</sub> is involved into the reaction. In this case, H<sub>2</sub>O<sub>2</sub> production was not terminated, indicating other O<sub>2</sub> source was responsible for the reaction. According to the XPS and O<sub>2</sub>-TPD results (Figs. 3g and 3h), O<sub>2</sub> could be adsorbed on the E-MoS<sub>2</sub>/FeS<sub>2</sub> surface. Therefore, the adsorbed O<sub>2</sub> also contributed to the H<sub>2</sub>O<sub>2</sub> production.

Based on above results, it was undoubtedly concluded that the H<sub>2</sub>O<sub>2</sub> was produced through two-step single-electron reduction (Eqs. 1-2), where  $\bullet O_2$  served as an intermediate. In Eqs. 1-2, the function of  $H^+$  is revealed by the increased H<sub>2</sub>O<sub>2</sub> yield following the decreased initial pH values (Fig. S9).

### 3.3.3. Positive role of -OH groups and SVs toward the H<sub>2</sub>O<sub>2</sub> production

We have plotted the number of modified -OH groups, the amount of



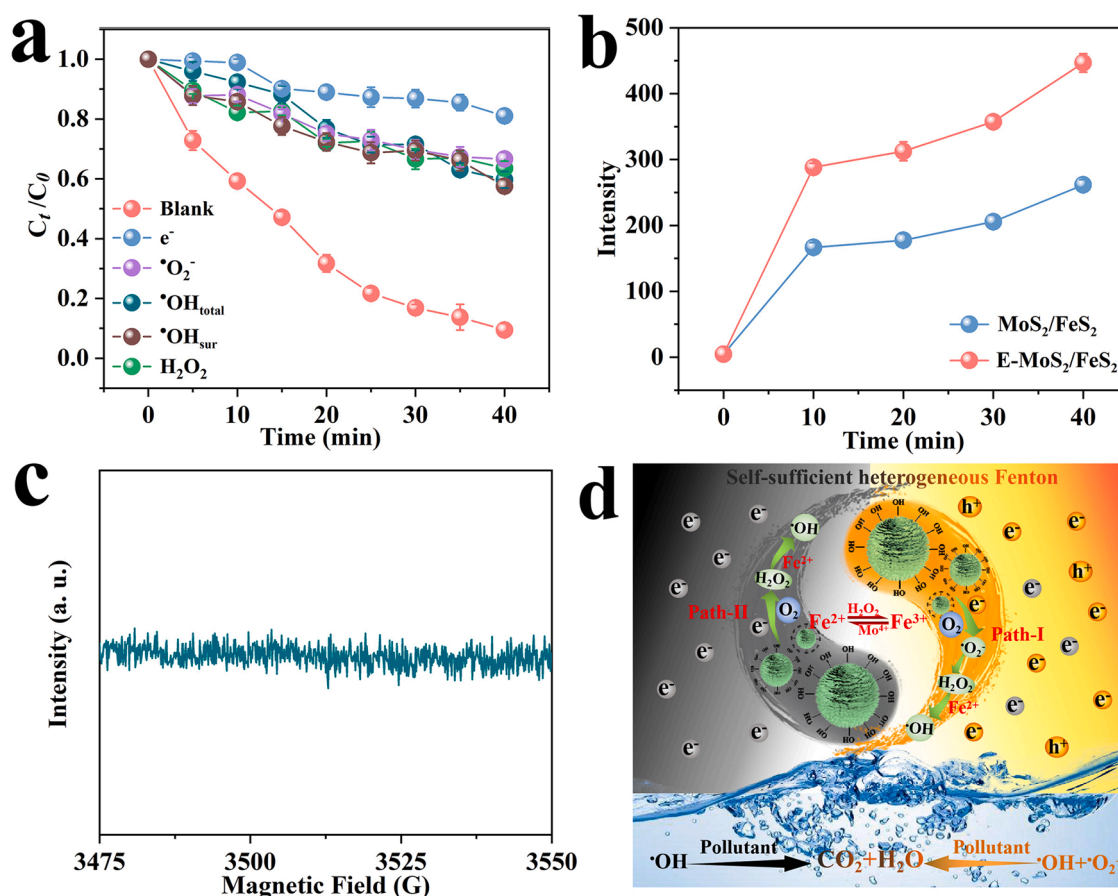


Fig. 7. (a) Radical trapping experiments for SSHF reaction catalyzed by E-MoS<sub>2</sub>/FeS<sub>2</sub>. (b) OH-TPA intensities for different systems over time. (c) EPR spectrum for DMPO- $\bullet OH$  in E-MoS<sub>2</sub>/FeS<sub>2</sub>. (d) SSHF reaction mechanism of E-MoS<sub>2</sub>/FeS<sub>2</sub>. Reaction condition: catalyst = 0.16 g/L, 50 mL [TC]<sub>0</sub> = 25 mg/L and initial pH = 6.5.

surface SVs, the yield of *in-situ* generated H<sub>2</sub>O<sub>2</sub> against the H<sub>2</sub>O<sub>2</sub>(pre) concentrations. As shown in Figs. 6b and S12, the variations of the modified -OH groups number and SVs amount are consistent with the *in-situ* generated H<sub>2</sub>O<sub>2</sub> yield, suggesting the important roles of -OH groups and SVs in *in-situ* H<sub>2</sub>O<sub>2</sub> production.

It is reported that -OH groups could function as internal scavengers for  $h^+$ , leading to an enhanced  $e^-$  separation efficiency [23,24]. The change of pH with reaction time during the SSHF reaction was monitored. As shown in Fig. S13, the pH of solution decreases as the reaction proceeds. On the one hand, some acidic intermediates ( $m/z = 256, 188, 170, 148, 116, 102, 74$ ) are generated in the SSHF reaction (Fig. S6). On the other hand, H<sup>+</sup> is released due to the internal  $h^+$ -scavenging effect of -OH groups [44,45]. To determine the internal  $h^+$ -scavenging effect, NaCl solution was replaced by Na<sub>2</sub>S solution (scavenger of  $h^+$ ) [46]. In Fig. 6c, the photocurrent variation of MoS<sub>2</sub>/FeS<sub>2</sub> + Vis system is more pronounced than that of E-MoS<sub>2</sub>/FeS<sub>2</sub> + Vis system, since the amount of the combined hole-electron pairs in the former system is higher before quenching  $h^+$ . This is also verified by photocurrent responses, where MoS<sub>2</sub>/FeS<sub>2</sub> displays higher response after quenching  $h^+$  by TEOA solution (Fig. 6d) [47]. Besides the  $e^-$  separation efficiency, the concentrations of intermediate  $\bullet O_2^-$  were also studied. In Fig. S11c, a higher signal intensity of DMPO- $\bullet O_2^-$  in E-MoS<sub>2</sub>/FeS<sub>2</sub> + Vis system is observed. Additionally, the NBT degradation efficiency over E-MoS<sub>2</sub>/FeS<sub>2</sub> + Vis system is also higher than that of MoS<sub>2</sub>/FeS<sub>2</sub> + Vis system (Fig. S11d). These results clearly indicated that more  $e^-$  were released, and participated into the  $\bullet O_2^-$  and H<sub>2</sub>O<sub>2</sub> formation with the help of internal  $h^+$ -scavenging effect via modified -OH groups.

Benefiting from the enhanced electron density, SVs could serve as another active sites for H<sub>2</sub>O<sub>2</sub> production (Eqs. 1–3). Different from the photocatalytic process, the H<sub>2</sub>O<sub>2</sub> production on SVs sites was

independent with visible light. As shown in Fig. 6a, H<sub>2</sub>O<sub>2</sub> yield over E-MoS<sub>2</sub>/FeS<sub>2</sub> reaches 0.2 mM/g/h in aqueous solution without visible light. H<sub>2</sub>O<sub>2</sub> production is terminated after quenching  $e^-$  by AgNO<sub>3</sub> solution, verifying the decisive role of  $e^-$  surrounding SVs toward the H<sub>2</sub>O<sub>2</sub> production in darkness. Surprisingly, in this case, the signal of DMPO- $\bullet O_2^-$  is undetected over E-MoS<sub>2</sub>/FeS<sub>2</sub> (Fig. S11c). This is also confirmed by the scarce NBT degradation (Fig. S11d). Therefore, it is inferred that one-step two-electron reduction were performed for H<sub>2</sub>O<sub>2</sub> production via  $e^-$  surrounding SVs (Eq. 3), where  $\bullet O_2^-$  was not functioned as an intermediate.

A radical trapping experiment was designed to estimate the contribution of H<sub>2</sub>O<sub>2</sub> generated by  $e^-$  surrounding SVs sites. In the presence of catalase (scavenger of H<sub>2</sub>O<sub>2</sub>) without visible light, the TC degradation efficiency within 90 min significantly decreases from 71.0 % (blank solution) to 16.4 % (Fig. S14), suggesting H<sub>2</sub>O<sub>2</sub> production and SSHF reaction are performed even in darkness. RhB is used as the pollutant, and the pink solution catalyzed by E-MoS<sub>2</sub>/FeS<sub>2</sub> becomes transparent in the night after 60 min (Video S1).

Supplementary material related to this article can be found online at [doi:10.1016/j.apcatb.2022.122307](https://doi.org/10.1016/j.apcatb.2022.122307).

### 3.3.4. Contribution of active species in TC degradation

After illustrating the *in-situ* H<sub>2</sub>O<sub>2</sub> production mechanism, the mechanism for subsequent heterogeneous Fenton reaction was investigated, and the radical trapping experiments were carried out to determine the possible active species in TC degradation. Firstly, the contribution of *in-situ* generated H<sub>2</sub>O<sub>2</sub> is studied using catalase as scavenger [48], and the efficiency decreases from 90.6 % (blank solution) to 36.5 % (Fig. 7a). TPA can be used as the fluorescence probe for  $\bullet OH$  [49]. The peak intensity of 2-hydroxy terephthalic acid (OH-TPA) at 375 nm increases

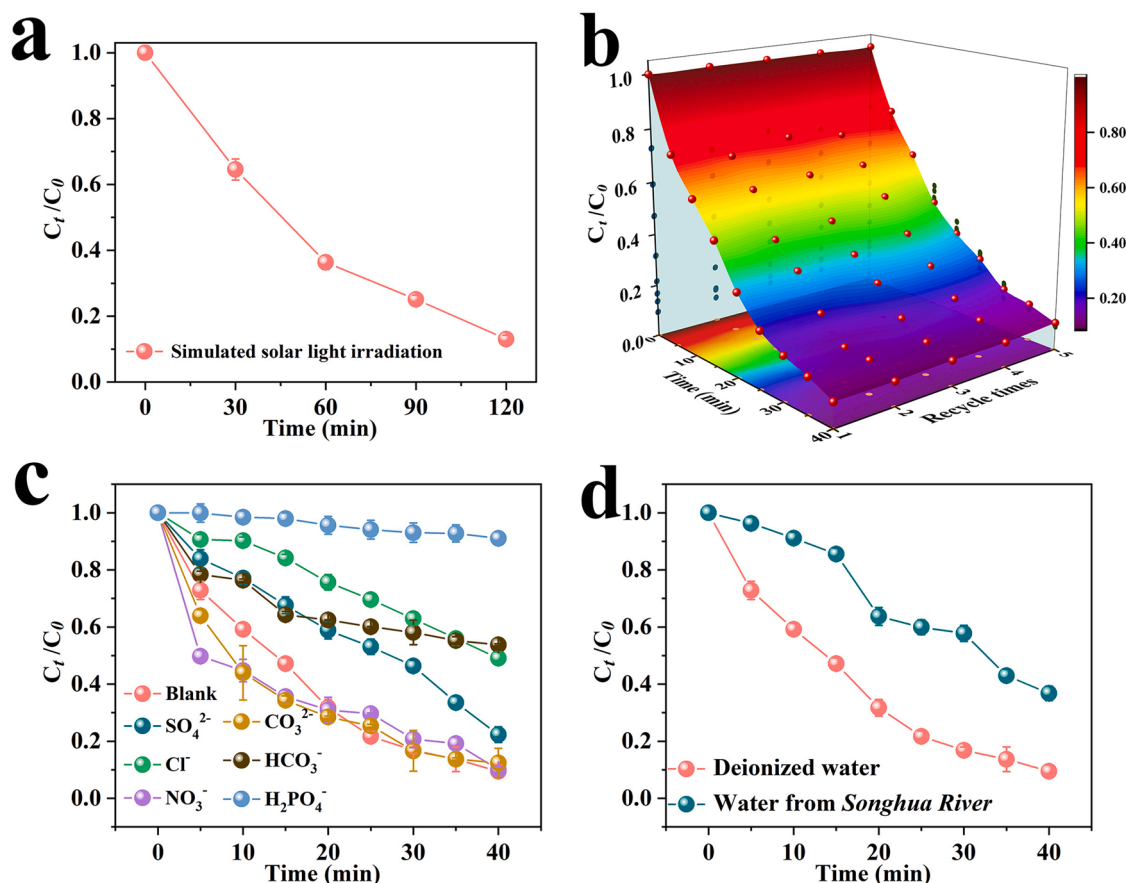


**Fig. 8.** SSHF reaction catalyzed by E-MoS<sub>2</sub>/FeS<sub>2</sub>: (a) TC degradation under simulated solar light. (b) Recycled experiments. (c) Impact of inorganic anions on degradation efficiency. (d) TC degradation processes in different solvents. Reaction condition: catalyst = 0.16 g/L, 50 mL [TC]<sub>0</sub> = 25 mg/L and initial pH = 6.5.

with the increased reaction times, indicating the *in-situ* generated H<sub>2</sub>O<sub>2</sub> was rapidly activated on the E-MoS<sub>2</sub>/FeS<sub>2</sub> surface (Fig. 7b). The peak intensity in E-MoS<sub>2</sub>/FeS<sub>2</sub> + Vis system is higher than that in MoS<sub>2</sub>/FeS<sub>2</sub> + Vis system due to the higher H<sub>2</sub>O<sub>2</sub> yield. Generally,  $\cdot\text{OH}_{\text{total}}$  were classified into surface-bonded  $\cdot\text{OH}$  ( $\cdot\text{OH}_{\text{sur}}$ ) and free  $\cdot\text{OH}$  in solution ( $\cdot\text{OH}_{\text{free}}$ ) [50]. Which one played a more important role? EPR measurement is susceptible to  $\cdot\text{OH}_{\text{free}}$ , however, the signal of DMPO- $\cdot\text{OH}_{\text{free}}$  is hardly observed in Fig. 7c, suggesting  $\cdot\text{OH}_{\text{free}}$  are scarcely produced. TBA was used to trap  $\cdot\text{OH}_{\text{total}}$ , and NaF was added to desorb  $\cdot\text{OH}_{\text{sur}}$  from the catalyst surface by forming " $\cdot\text{OH}\cdots\text{F}$ " hydrogen bond [51,52]. In Fig. 7a, their quenching effects are similar, indicating that SSHF reaction mainly performs on the catalyst surface.

Next, the contributions of  $\cdot\text{OH}_{\text{total}}$ ,  $\cdot\text{O}_2$ , and  $e^-$  are investigated using TBA, BQ, and AgNO<sub>3</sub> as the scavengers (Fig. 7a), and the efficiencies respectively decrease to 40.3 %, 33.4 %, and 19.0 %, indicating their contributions follow the order:  $e^- > \cdot\text{O}_2 > \cdot\text{OH}_{\text{total}}$ . Compared to the heterogeneous Fenton reaction, where  $\cdot\text{OH}_{\text{total}}$  acted as the crucial active species [53], the contributions of  $e^-$  and  $\cdot\text{O}_2$  in SSHF reaction were higher, since  $e^-$  and  $\cdot\text{O}_2$  directly involved into the *in-situ* H<sub>2</sub>O<sub>2</sub> production (Eqs. 1–3). According to the dominating contributions of  $e^-$  and  $\cdot\text{O}_2$ , we could infer that H<sub>2</sub>O<sub>2</sub> yield played a decisive role. And this further confirmed that H<sub>2</sub>O<sub>2</sub> production process was the rate-limiting step in SSHF reaction.

### 3.3.5. SSHF reaction mechanism

Based on the above analysis, a possible catalytic mechanism of Z-scheme E-MoS<sub>2</sub>/FeS<sub>2</sub> heterojunction is shown in Fig. 5c. Under visible light,  $e^-$  and  $h^+$  respectively accumulated on the CB of FeS<sub>2</sub> and the VB of MoS<sub>2</sub>. The CB of FeS<sub>2</sub> was -0.51 eV, therefore,  $e^-$  was powerful enough to reduce O<sub>2</sub> to be  $\cdot\text{O}_2$  and H<sub>2</sub>O<sub>2</sub> (Eqs. 1–2). Benefiting from the internal

$h^+$ -scavenging effect of modified -OH groups, the  $e^-$  separation efficiency was improved, leading to an enhanced H<sub>2</sub>O<sub>2</sub> yield. Besides the photocatalytic synthesis, H<sub>2</sub>O<sub>2</sub> could also be produced via  $e^-$  surrounding SVs even in darkness (Eq. 3). Coupling these dual production paths, the *in-situ* generated H<sub>2</sub>O<sub>2</sub> amount is sufficient for the Fenton reaction, and they were rapidly activated to be  $\cdot\text{OH}_{\text{sur}}$  for TC degradation (Fig. 7d). Besides  $\cdot\text{OH}_{\text{sur}}$ , other reactive species generated in the photocatalytic process, including  $e^-$  and  $\cdot\text{O}_2$ , were also involved in TC degradation. Benefiting from these multiple reactive species, 86.9 % of TC is degraded under simulated solar light within 120 min (Fig. 8a), and the pollutant RhB is quickly faded under actual sunlight within 25 min (Video S2).

Supplementary material related to this article can be found online at [doi:10.1016/j.apcatb.2022.122307](https://doi.org/10.1016/j.apcatb.2022.122307).

### 3.4. Recyclability and practical application ability

The recyclability was necessary to evaluate the catalytic performance. After 5 cycles, nearly 76.9 % of TC degradation efficiency is preserved (Fig. 8b), indicating E-MoS<sub>2</sub>/FeS<sub>2</sub> displays satisfying recyclability. The leaching of iron and molybdenum ions is measured by ICP measurement, and the values are only 0.129 and 0.183 mg/L, respectively. Even in acidic and alkaline conditions (Fig. S15a), the values completely meet the quality standards of European Union and China (GB/T 31962-2015) [54,55]. In comparison with the fresh sample, the morphology, structure, and crystalline phase of the recycled one are almost unchanged (Figs. S15b-S15d). Additionally, the composition stability was tested by XPS measurement (Fig. S16). The core-level spectra of Fe 2p and S 2p are similar before and after SSHF reaction. The content of Mo<sup>6+</sup> increases from 19.7 % to 25.3 % due to the oxidation by radicals. The amount of -OH groups increases from 36.0 %

to 44.6 % after the reaction owing to the generation of  $\bullet\text{OH}_{\text{sur}}$  on the surface.

Inorganic anions ubiquitously exist in water system, and their influence on degradation efficiency was studied. Herein, several common anions, including  $\text{H}_2\text{PO}_4^-$ ,  $\text{HCO}_3^-$ ,  $\text{CO}_3^{2-}$ ,  $\text{NO}_3^-$ ,  $\text{Cl}^-$ , and  $\text{SO}_4^{2-}$  are selected (Fig. 8c). In the presence of  $\text{NO}_3^-$  and  $\text{CO}_3^{2-}$ , little influence on degradation efficiency is visible. With the addition of  $\text{HCO}_3^-$ ,  $\text{Cl}^-$ ,  $\text{SO}_4^{2-}$ , and  $\text{H}_2\text{PO}_4^-$ , the efficiency decreases to 46.2 %, 51.0 %, 77.7 %, and 9.0 %, which is attributed to their quenching effect toward  $\bullet\text{OH}_{\text{total}}$  and the destruction of active  $\text{Fe}^{2+}$  sites [56,57]. To evaluate the practicability, TC solution is prepared using water from the *Songhua River* to replace deionized water, and the degradation efficiency is 63.2 % within 40 min (Fig. 8d).

#### 4. Conclusions

In this study, a Z-scheme E-MoS<sub>2</sub>/FeS<sub>2</sub> heterojunction with plenty of -OH groups and SVs on the surface was prepared. In SSHF reaction, 1.5 mM/g/h of H<sub>2</sub>O<sub>2</sub> was generated in neutral aqueous solution without external  $h^+$  scavenger, much higher than those of the reference catalysts. Mechanism studies indicated that H<sub>2</sub>O<sub>2</sub> was produced via dual paths: two-step single-electron reduction by  $e^-$  on CB of FeS<sub>2</sub> during the photocatalytic process, where the internal  $h^+$ -scavenging effect of -OH groups was contributed for the enhanced  $e^-$  separation efficiency and increased H<sub>2</sub>O<sub>2</sub> yield. Additionally,  $e^-$  surrounding SVs were also responsible for H<sub>2</sub>O<sub>2</sub> production through one-step two-electron reduction even in darkness. Benefiting from dual production paths, the H<sub>2</sub>O<sub>2</sub> yield was maximized, and was enough for the subsequent Fenton reaction. As a result, TC degradation rate was  $5.9 \times 10^{-2} \text{ min}^{-1}$ , about 5.3 times higher than that of MoS<sub>2</sub>/FeS<sub>2</sub>, and was even comparable to heterogeneous Fenton reaction. Radical trapping experiments indicated that  $e^-$  and  $\bullet\text{O}_2^-$  displayed the greatest contributions in SSHF reaction, and this was different from the heterogeneous Fenton reaction, whose main active species was  $\bullet\text{OH}_{\text{total}}$ . The findings were favorable for the SSHF catalyst design, and maybe extended to explore other outstanding catalysts with higher *in-situ* H<sub>2</sub>O<sub>2</sub> yield and better degradation performance.

#### CRediT authorship contribution statement

Yang Yang: Data curation, Validation, Writing – review & editing, Formal analysis, Haochen Yu: Data curation, Validation, Maoquan Wu: Validation, Tingting Zhao: Data curation, Yina Guan: Data curation, Dong Yang: Validation, Yufeng Zhu: Investigation, Yanqiu Zhang: Data curation, Shouchun Ma: Data curation, Jie Wu: Resources, Funding acquisition, Li Liu: Resources, Conceptualization, Funding acquisition, Tongjie Yao: Supervision, Conceptualization, Writing – review & editing, Funding acquisition.

#### Declaration of Competing Interest

The authors declare that they have no known competing financial interests or personal relationships that could have appeared to influence the work reported in this paper.

#### Data availability

Data will be made available on request.

#### Acknowledgements

This work was supported by the National Natural Science Foundation of China (21674028); State Key Laboratory of Urban Water Resource and Environment (Harbin Institute of Technology, No. 2022TS40); Fundamental Research Funds for Heilongjiang Province Universities (KJCX201911).

#### Appendix A. Supporting information

Supplementary data associated with this article can be found in the online version at doi:10.1016/j.apcatb.2022.122307.

#### References

- [1] Q.Y. Yan, C. Lian, K. Huang, L.H. Liang, H.R. Yu, P.C. Yin, J.L. Zhang, M.Y. Xing, Constructing an acidic microenvironment by MoS<sub>2</sub> in heterogeneous fenton reaction for pollutant control, *Angew. Chem. Int. Ed.* 60 (2021) 17155–17163.
- [2] D.L. Yuan, C. Zhang, S.F. Tang, X. Li, J.C. Tang, Y.D. Rao, Z.B. Wang, Q.R. Zhang, Enhancing CaO<sub>2</sub> fenton-like process by Fe(II)-oxalic acid complexation for organic wastewater treatment, *Water Res.* 163 (2019), 114861.
- [3] X.J. Yang, X.M. Xu, J. Xu, Y.F. Han, Iron oxychloride (FeOCl): an efficient fenton-like catalyst for producing hydroxyl radicals in degradation of organic contaminants, *J. Am. Chem. Soc.* 135 (2013) 16058–16061.
- [4] Y. Liu, Y. Zhao, J.L. Wang, Fenton/Fenton-like processes with in-situ production of hydrogen peroxide/hydroxyl radical for degradation of emerging contaminants: advances and prospects, *J. Hazard. Mater.* 404 (2021), 124191.
- [5] Z. Yang, X. Zhang, S. Pu, R. Ni, Y. Lin, Y. Liu, Novel Fenton-like system (Mg/Fe-O<sub>2</sub>) for degradation of 4-chlorophenol, *Environ. Pollut.* 250 (2019) 906–913.
- [6] C.R. Dong, Y.L. Yang, X.M. Hu, Y.J. Cho, G.Y. Jang, Y.H. Ao, L.Y. Wang, J.Y. Shen, J.H. Park, K. Zhang, Self-cycled photo-Fenton-like system based on an artificial leaf with as low-to-H<sub>2</sub>O<sub>2</sub> conversion efficiency of 1.46%, *Nat. Commun.* 13 (2022) 4982.
- [7] Y.X. Li, S.X. Ouyang, H. Xu, X. Wang, Y.P. Bi, Y.F. Zhang, J.H. Ye, Constructing solid-gas-interfacial fenton reaction over alkalized-C<sub>3</sub>N<sub>4</sub> photocatalyst to achieve apparent quantum yield of 49% at 420 nm, *J. Am. Chem. Soc.* 138 (2016) 13289–13297.
- [8] G.H. Moon, S. Kim, Y.J. Cho, J. Lim, D.H. Kim, W.Y. Choi, Synergistic combination of bandgap-modified carbon nitride and WO<sub>3</sub> for visible light-induced oxidation of arsenite accelerated by in-situ Fenton reaction, *Appl. Catal. B: Environ.* 218 (2017) 819–824.
- [9] Y. Wu, J. Chen, H.N. Che, X. Gao, Y.H. Ao, P.F. Wang, Boosting 2e<sup>-</sup> oxygen reduction reaction in garland carbon nitride with carbon defects for high-efficient photocatalysis-self-Fenton degradation of 2,4-dichlorophenol, *Appl. Catal. B: Environ.* 307 (2022), 121185.
- [10] J. Ma, K. Wang, C. Wang, X.J. Chen, W. Zhu, G.X. Zhu, W.Q. Yao, Y.F. Zhu, Photocatalysis-self-Fenton system with high-fluent degradation and high mineralization ability, *Appl. Catal. B: Environ.* 276 (2020), 119150.
- [11] F. Wang, J. Xu, Z.P. Wang, Y. Lou, C.S. Pan, Y.F. Zhu, Unprecedentedly efficient mineralization performance of photocatalysis-self-Fenton system towards organic pollutants over oxygen-doped porous g-C<sub>3</sub>N<sub>4</sub> nanosheets, *Appl. Catal. B: Environ.* 312 (2022), 121438.
- [12] J. Zhang, G. Zhang, Q.H. Ji, H.C. Lan, J.H. Qu, H.J. Liu, Carbon nanodot-modified FeOCl for photo-assisted Fenton reaction featuring synergistic in-situ H<sub>2</sub>O<sub>2</sub> production and activation, *Appl. Catal. B: Environ.* 266 (2020), 118665.
- [13] Y. Hu, Z. Zhong, M.T. Lu, Y. Muhammad, S.J. Shah, H. He, W.X. Gong, Y.F. Ren, X. Yu, Z.X. Zhao, Biomimetic O<sub>2</sub>-carrying and highly in-situ H<sub>2</sub>O<sub>2</sub> generation using Ti<sub>3</sub>C<sub>2</sub>MXene/MIL-100(Fe) hybrid via Fe-Protoporphyrin bridging for photo-fenton synergistic degradation of thiachlorid, *Chem. Eng. J.* 450 (2022), 137964.
- [14] Y.P. Zhu, R.L. Zhu, Y.F. Xi, J.X. Zhu, G.Q. Zhu, H.P. He, Strategies for enhancing the heterogeneous Fenton catalytic reactivity: a review, *Appl. Catal. B: Environ.* 255 (2019), 117739.
- [15] M.S. Hosseini, A. Abbasi, M. Masteri-Farhani, Improving the photocatalytic activity of NH<sub>2</sub>-UiO-66 by facile modification with Fe(acac)<sub>3</sub> complex for photocatalytic water remediation under visible light illumination, *J. Hazard. Mater.* 425 (2022), 127975.
- [16] G.P. Zhu, X.D. Yu, F. Xie, W. Feng, Ultraviolet light assisted heterogeneous Fenton degradation of tetracycline based on polyhedral Fe<sub>3</sub>O<sub>4</sub> nanoparticles with exposed high-energy {110} facets, *Appl. Surf. Sci.* 485 (2019) 496–505.
- [17] X. Nie, G.Y. Li, S.S. Li, Y.M. Luo, W.M. Luo, Q. Wan, T.C. An, Highly efficient adsorption and catalytic degradation of ciprofloxacin by a novel heterogeneous Fenton catalyst of hexapod-like pyrite nanosheets mineral clusters, *Appl. Catal. B: Environ.* 300 (2022), 120734.
- [18] J. Hang, X.H. Yi, C.C. Wang, H.F. Fu, P. Wang, Y.J. Zhao, Heterogeneous photo-Fenton degradation toward sulfonamide matrix over magnetic Fe<sub>3</sub>S<sub>4</sub> derived from MIL-100(Fe), *J. Hazard. Mater.* 424 (2022), 127415.
- [19] W.J. An, H. Wang, T. Yang, J.F. Xu, Y.S. Wang, D. Liu, J.S. Hu, W.Q. Cui, Y. H. Liang, Enriched photocatalysis-Fenton synergistic degradation of organic pollutants and coking wastewater via surface oxygen vacancies over Fe-BiOBr composites, *Chem. Eng. J.* 451 (2023), 138653.
- [20] C. Krishnaraj, H.S. Jena, L. Bourda, A. Laemont, P. Pachfule, J. Roesser, C. V. Chandran, S. Borgmans, S.M.J. Rogge, K. Leus, C.V. Stevens, J.A. Martens, V. V. Speybroeck, E. Breynaert, A. Thomas, P.V.D. Voort, Strongly reducing (diaryl amino)benzene-based covalent organic framework for metal-free visible light photocatalytic H<sub>2</sub>O<sub>2</sub> generation, *J. Am. Chem. Soc.* 142 (2020) 20107–20116.
- [21] H. Zhang, M. Liu, X.Y. Zhang, B. Yuan, P. Wu, C.J. Liu, W. Jiang, On-site H<sub>2</sub>O<sub>2</sub> production with amphiphilic g-C<sub>3</sub>N<sub>4</sub> as photocatalyst in a combined photocatalysis-extraction-separation process, *Chem. Eng. J.* 438 (2022), 135664.



- [22] G.D. Chen, J. Feng, W.S. Wang, Y.D. Yin, H.Z. Liu, Photocatalytic removal of hexavalent chromium by newly designed and highly reductive TiO<sub>2</sub> nanocrystals, *Water Res* 108 (2017) 383–390.
- [23] R.R. Jiang, G.H. Lu, Z.H. Yan, J.C. Liu, D.H. Wu, Y.H. Wang, Microplastic degradation by hydroxy-rich bismuth oxychloride, *J. Hazard. Mater.* 405 (2021), 124247.
- [24] X.Y. Wang, X.Y. Li, J.C. Mu, S.Y. Fan, X. Chen, L. Wang, Z.F. Yin, M. Tadé, S.M. Liu, Oxygen vacancy-rich porous Co<sub>3</sub>O<sub>4</sub> nanosheets toward boosted NO reduction by CO and CO oxidation: insights into the structure-activity relationship and performance enhancement mechanism, *ACS Appl. Mater. Interfaces* 11 (2019) 41988–41999.
- [25] G.Q. Li, D. Zhang, Q. Qiao, Y.F. Yu, D. Peterson, A. Zafar, R. Kumar, S. Curtarolo, F. Hunte, S. Shannon, Y.M. Zhu, W.T. Yang, L.Y. Cao, All the catalytic active sites of MoS<sub>2</sub> for hydrogen evolution, *J. Am. Chem. Soc.* 138 (2016) 16632–16638.
- [26] Y.J. Luo, P. Shen, X.C. Li, Y.L. Guo, K. Chu, Sulfur-deficient Bi<sub>2</sub>S<sub>3-x</sub> synergistically coupling Ti<sub>3</sub>C<sub>2</sub>T<sub>x</sub>-MXene for boosting electrocatalytic N<sub>2</sub> reduction, *Nano Res* 15 (2022) 3991–3999.
- [27] J.X. Ni, W. Wang, D.M. Liu, Q. Zhu, J.L. Jia, J.Y. Tian, Z.Y. Li, X. Wang, Z.P. Xing, Oxygen vacancy-mediated sandwich-structural TiO<sub>2-x</sub>/ultrathin g-C<sub>3</sub>N<sub>4</sub>/TiO<sub>2-x</sub> direct Z-scheme heterojunction visible-light-driven photocatalyst for efficient removal of high toxic tetracycline antibiotics, *J. Hazard. Mater.* 408 (2021), 124432.
- [28] B.H. Qin, Y.H. Li, H.J. Wang, G.X. Yang, Y.H. Cao, H. Yu, Q. Zhang, H. Liang, F. Peng, Efficient electrochemical reduction of CO<sub>2</sub> into CO promoted by sulfur vacancies, *Nano Energy* 60 (2019) 43–51.
- [29] Y. Xu, M. Wang, Q. Xie, Y.Y. Wang, X.J. Cui, L.H. Jiang, B-Zn<sub>2</sub>Cd<sub>1-x</sub>S/Cd heterojunction with sulfur vacancies for photocatalytic overall dyeing wastewater splitting, *ACS Sustain. Chem. Eng.* 10 (2022) 2938–2946.
- [30] Z. Chen, D.C. Yao, C.C. Chu, S. Mao, Photocatalytic H<sub>2</sub>O<sub>2</sub> production systems: design strategies and environmental applications, *Chem. Eng. J.* 451 (2023), 138489.
- [31] Y.N. Xu, X.J. Guo, F. Zha, X.H. Tang, H.F. Tian, Efficient photocatalytic removal of orange II by a Mn<sub>3</sub>O<sub>4</sub>-FeS<sub>2</sub>/Fe<sub>2</sub>O<sub>3</sub> heterogeneous catalyst, *J. Environ. Manag.* 253 (2020), 109695.
- [32] C. Kong, F.J. Zhang, Y.R. Wang, J. Huang, Synthesis and photocatalytic hydrogen activity of Mo<sub>1-x</sub>S<sub>2</sub> nanosheets with controllable Mo vacancies, *J. Alloy. Compd.* 876 (2021), 160165.
- [33] C.C. Chu, Q.J. Li, W. Miao, H.H. Qin, X.R. Liu, D.C. Yao, S. Mao, Photocatalytic H<sub>2</sub>O<sub>2</sub> production driven by cyclodextrin-pyrimidine polymer in a wide pH range without electron donor or oxygen aeration, *Appl. Catal. B: Environ.* 314 (2022), 121485.
- [34] R. Yamaguchi, S. Kurosu, M. Suzuki, Y. Kawase, Hydroxyl radical generation by zero-valent iron/Cu (ZVI/Cu) bimetallic catalyst in wastewater treatment: heterogeneous Fenton/Fenton-like reactions by Fenton reagents formed in-situ under oxic conditions, *Chem. Eng. J.* 334 (2018) 1537–1549.
- [35] X. Liu, P. Xu, S.Q. Xie, L. Wang, Z.Y. Yang, P.F. Zhu, J.W. Ma, Q.L. He, J. C. Crittenden, Multiple reinforcement of chloride ion on oxidizing acetaminophen with zero-valent copper particles: in-situ formation and catalysis of hydrogen peroxide, *Chem. Eng. J.* 451 (2023), 138689.
- [36] Y.P. Zhu, R.L. Zhu, Y.F. Xi, J.X. Zhu, G.Q. Zhu, H.P. He, Strategies for enhancing the heterogeneous Fenton catalytic reactivity: a review, *Appl. Catal. B: Environ.* 255 (2019), 117739.
- [37] Y.M. Zheng, Y. Luo, Q.S. Ruan, J. Yu, X.L. Guo, W.J. Zhang, H. Xie, Z. Zhang, J. J. Zhao, Y. Huang, Plasma-tuned nitrogen vacancy graphitic carbon nitride sphere for efficient photocatalytic H<sub>2</sub>O<sub>2</sub> production, *J. Colloid Interf. Sci.* 609 (2022) 75–85.
- [38] C. Bao, H. Zhang, L.C. Zhou, Y.M. Shao, J.J. Ma, Q. Wu, Preparation of copper doped magnetic porous carbon for removal of methylene blue by a heterogeneous Fenton-like reaction, *RSC Adv.* 5 (2015) 72423–72432.
- [39] Z. Wei, M.L. Liu, Z.J. Zhang, W.Q. Yao, H.W. Tan, Y.F. Zhu, Efficient visible-light-driven selective oxygen reduction to hydrogen peroxide by oxygen-enriched graphitic carbon nitride polymers, *Energy Environ. Sci.* 11 (2018) 2581.
- [40] C.W. Du, W.W. Feng, S.Y. Nie, J.L. Zhang, Y.T. Liang, X. Han, Y.H. Wu, J.L. Feng, S. Y. Dong, H.J. Liu, J.H. Sun, Harnessing efficient in-situ H<sub>2</sub>O<sub>2</sub> production via a KPF<sub>6</sub>/BiOBr photocatalyst for the degradation of polyethylene, *Sep. Purif. Technol.* 279 (2021), 119734.
- [41] J.S. Liu, B.J. Wang, Z.Q. Li, Z.Y. Wu, K.J. Zhu, Photo-Fenton reaction and H<sub>2</sub>O<sub>2</sub> enhanced photocatalytic activity of α-Fe<sub>2</sub>O<sub>3</sub> nanoparticles obtained by a simple decomposition route, *J. Alloy. Compd.* 771 (2019) 398–405.
- [42] H.Y. Song, L.S. Wei, C.X. Chen, C.C. Wen, F.Q. Han, Photocatalytic production of H<sub>2</sub>O<sub>2</sub> and its in situ utilization over atomic-scale Au modified MoS<sub>2</sub> nanosheets, *J. Catal.* 376 (2019) 198–208.
- [43] A. Galinska, J. Walendziewski, Photocatalytic water splitting over Pt-TiO<sub>2</sub> in the presence of sacrificial reagents, *Energy Fuels* 19 (2005) 1143–1147.
- [44] L. Zhou, J.Y. Lei, F.C. Wang, L.Z. Wang, M.R. Hoffmann, Y.D. Liu, S. In, J.L. Zhang, Carbon nitride nanotubes with in situ grafted hydroxyl groups for highly efficient spontaneous H<sub>2</sub>O<sub>2</sub> production, *Appl. Catal. B: Environ.* 288 (2021), 119993.
- [45] C. Chen, G.H. Qiu, T. Wang, Z.Q. Zheng, M.T. Huang, B.X. Li, Modulating oxygen vacancies on bismuth-molybdate hierarchical hollow microspheres for photocatalytic selective alcohol oxidation with hydrogen peroxide production, *J. Colloid Interface Sci.* 592 (2021) 1–12.
- [46] A. Helal, F.A. Harraz, A.A. Ismail, T.M. Sami, I.A. Ibrahim, Hydrothermal synthesis of novel heterostructured Fe<sub>2</sub>O<sub>3</sub>/Bi<sub>2</sub>S<sub>3</sub> nanorods with enhanced photocatalytic activity under visible light, *Appl. Catal. B: Environ.* 213 (2017) 18–27.
- [47] S.Q. Huang, Y.G. Xu, T. Zhou, M. Xie, Y. Ma, Q.Q. Liu, L.Q. Jing, H. Xu, H.M. Li, Constructing magnetic catalysts with in-situ solid-liquid interfacial photo-Fenton-like reaction over Ag<sub>3</sub>PO<sub>4</sub>@NiFe<sub>2</sub>O<sub>4</sub> composites, *Appl. Catal. B: Environ.* 225 (2018) 40–50.
- [48] W. Cai, S. Wu, Y. Liu, D. Li, A novel Prussian blue-magnetite composite synthesized by self-template method and its application in reduction of hydrogen peroxide, *Appl. Organomet. Chem.* 32 (2018) 3909.
- [49] Y. Yang, Q.Q. Wang, R. Aleisa, T.T. Zhao, S.C. Ma, G.X. Zhang, T.J. Yao, Y.D. Yin, MoS<sub>2</sub>/FeS nanocomposite catalyst for efficient fenton reaction, *ACS Appl. Mater. Interfaces* 13 (2021) 51829–51838.
- [50] J. Liu, Y.M. Yue, W. Wang, F.T. Tan, H.L. Xia, X.Y. Wang, X.L. Qiao, P.K. Wong, Facile one-step synthesis of 3D hierarchical flower-like magnesium peroxide for efficient and fast removal of tetracycline from aqueous solution, *J. Hazard. Mater.* 397 (2020), 122877.
- [51] Yi.M. Xu, K. Lv, Z.G. Xiong, W.H. Leng, W.P. Du, D. Liu, X.J. Xue, Rate enhancement and rate inhibition of phenol degradation over irradiated anatase and rutile TiO<sub>2</sub> on the addition of NaF: new insight into the mechanism, *J. Phys. Chem. C* 111 (2007) 19024–19032.
- [52] H.W. Tian, M. Liu, W.T. Zheng, Constructing 2D graphitic carbon nitride nanosheets/layered MoS<sub>2</sub>/graphene ternary nanojunction with enhanced photocatalytic activity, *Appl. Catal. B: Environ.* 225 (2018) 468–476.
- [53] M.Y. Xing, W.J. Xu, C.C. Dong, Y.C. Bai, J.B. Zeng, Y. Zhou, J.L. Zhang, Y.D. Yin, Metal sulfides as excellent Co-catalysts for H<sub>2</sub>O<sub>2</sub> decomposition in advanced oxidation processes, *Chem* 4 (2018) 1–14.
- [54] J.T. Tang, J.L. Wang, Metal organic framework with coordinatively unsaturated sites as efficient Fenton-like catalyst for enhanced degradation of sulfamethazine, *Environ. Sci. Technol.* 52 (2018) 5367–5377.
- [55] X.H. Deng, W.T. Hui, Y.N. Guan, Y.Q. Zhang, T.T. Zhao, C.L. Guo, B.F. Xin, Y. Yang, T.J. Yao, J. Wu, A nanoreactor with Z-scheme FeS<sub>2</sub>/MoS<sub>2</sub> heterojunctions encapsulated inside the carbon capsule: Insight on preparation method and enhanced performance in photo-Fenton reaction, *Chem. Eng. J.* 450 (2022), 138221.
- [56] Y.X. Wang, L. Rao, P.F. Wang, Z.Y. Shi, L.X. Zhang, Photocatalytic activity of N-TiO<sub>2</sub>/O-doped N vacancy g-C<sub>3</sub>N<sub>4</sub> and the intermediates toxicity evaluation under tetracycline hydrochloride and Cr(VI) coexistence environment, *Appl. Catal. B: Environ.* 262 (2020), 118308.
- [57] L.M. Hu, G.S. Zhang, M. Liu, Q. Wang, P. Wang, Enhanced degradation of Bisphenol A (BPA) by peroxymonosulfate with Co<sub>3</sub>O<sub>4</sub>-Bi<sub>2</sub>O<sub>3</sub> catalyst activation: Effects of pH, inorganic anions, and water matrix, *Chem. Eng. J.* 338 (2018) 300–310.